



Research Article

Property manipulation of CoCrFeNiAlCu high-entropy alloy under GPa high pressure



Xiaohong Wang, Huiqing Xie, Yulei Deng, Dongdong Zhu *, Xing Yang, Duo Dong, Tengfei Ma *

Key Laboratory of Air-driven Equipment Technology of Zhejiang Province, Quzhou University, Quzhou 324000, China

ARTICLE INFO

Article history:

Received 1 September 2022

Received in revised form 23 November 2022

Accepted 16 December 2022

Available online 17 December 2022

Keywords:

High pressure

High entropy alloy

Segregation regulation

Corrosion

Nanohardness

ABSTRACT

In this study, we investigated the corrosion resistance and mechanical properties of a $\text{CoCrFeNiAl}_{0.2}\text{Cu}_{0.8}$ high-entropy alloy (HEA) that was subjected to high-pressure solidification at 4 and 7 GPa. In addition, the mechanism of the effect of Cu segregation regulation on the properties was described. Results indicated that the volume fraction of the Cu-enriched FCC2 phase segregated at the grain boundary decreased from 8.17 % to 5.42 % under high pressure. We also observed that high-pressure solidification can lead to the formation of nano-precipitates in the FCC2 phase with better refinement and distribution uniformity. The reduction in the Cu-enriched FCC2 phase led to a decrease in the corrosion rate by approximately 85.6 % with an increased solidification pressure of 7 GPa, thereby improving corrosion resistance. Finally, we achieved a superior hardness and yield strength combination via fine-scale nano-precipitates and solution strengthening.

© 2022 Elsevier B.V. All rights reserved.

1. Introduction

Compared to traditional alloys, high-entropy alloys (HEAs) have high strength [1,2], high-temperature oxidation resistance [3–5], corrosion resistance [6–8], and wear resistance [9–11], etc. They are considered a new type of structural and functional material for a wide range of potential applications. For example, HEAs with excellent corrosion resistance and high strength are in high demand, because the materials used in the transportation of oil, natural gas, and chemical liquids are exposed to harsh conditions; therefore, HEAs with excellent corrosion resistance would be ideal for these applications. Cu is often added to HEAs due to its ubiquity, and its effects on the hardness, wear, and corrosion resistance [12–16] of the alloy. However, the average enthalpy of mixing for Cu in most HEAs is positive, which increases the probability that it will be repelled from the solid solution, thereby promoting segregation at the grain boundaries [17,18]. For example, the enthalpy of mixing of Cu, Al, Co, Cr, Fe, and Ni in the CoCrFeNiAlCu alloy is 5.67, -10.5, -3, -1.67, -0.33, and -4.5 KJ/mol, respectively. Segregation at the grain boundary weakens grain bonding and decreases corrosion resistance. Chen et al. [19] found that with increased Cu content, the Al and Cu rich precipitates in the $\text{Al}_{0.3}\text{Cu}_x\text{CoCrFeNi}$ alloys emerged gradually, resulting in decreased corrosion resistance and the

weakening of the passive film. Intergranular corrosion (IGC) was also observed in Cu-containing Al-Mg-Si alloys [20]. The IGC susceptibility in these alloys was closely related to the Si: Mg ratio as well as the Cu content [21–24].

Based on this review of the literature, we propose an ultrahigh-pressure preparation method to prevent Cu segregation. When metals or alloys are solidified under high pressure, the morphology, phase composition, and solid solubility of their solid–liquid interface are impacted [25–27], due to changes in the solute diffusion coefficient, equilibrium distribution coefficient, surface tension, and crystal growth rate. For example, the solid solubility of Si in α -Al increased from 0.15 wt% to 8.26 wt% when the Al hypoeutectic alloy containing 9.21 wt% Si was solidified at high-pressure [28]. The dispersed strengthening phase precipitated more easily in the subsequent heat-treatment process, indicating that the properties of the alloy prepared under high pressure were markedly improved [29,30]. Chang et al. [31] examined the microstructural evolution of FeCoNiAlSi HEAs under high-pressure solidification and found that the volume fraction of the grain boundary and peritectic phases decreased at 7 GPa. Chang et al. [32] also found that FeCoNi alloys solidified at 4 GPa showed hardening of the grain boundary phases. The use of high pressure increased the density of the alloy after solidification, which reduced vacancy defects as well as the degree of elemental segregation. Based on these studies, high-pressure preparation of HEAs is an effective means to eliminate segregation, increase corrosion resistance, and improve mechanical properties.

* Corresponding authors.

E-mail addresses: zhudd8@163.com (D. Zhu), matengfeihit@163.com (T. Ma).

In this study, we prepared CoCrFeNiAlCu HEAs under various high-pressure conditions (ambient pressure, 4 GPa, and 7 GPa). Then, we analyzed the alloy microstructure, phase composition, elemental distribution, and corrosion performance of each HEA. Based on these analyses, we established a mechanism for the high-pressure regulation of alloy corrosion performance, which provides new insights into the preparation of HEA materials with high corrosion resistance and good mechanical performance.

2. Experimental and methods

The CoCrFeNiAl_{0.2}Cu_{0.8} alloy was synthesized using vacuum arc melting of pure Al, Co, Cr, Cu, Fe, and Ni (purity of 99.99 %). The sample was then cut into cylinders (Φ 3 mm \times 3.7 mm) using wire cutting, followed by grinding and polishing. A high-pressure solidification test was performed using the Max Voggereiter high-temperature/high-pressure hydraulic press (LPR1000–400/50). During the HEA synthesis, a graphite tube was used as the heating furnace, pyrophyllite was used as the packaging material and pressure transmission medium, and zirconia was used as the insulation layer. The HEA sample was then placed in a chamber, where the pressure was increased to the desired value (4 or 7 GPa). Under the high-pressure condition, the temperature was increased to 1800 K over the course of 1 h. The temperature was held at 1800 K for 15 min and then cooled to 25 °C, where the pressure was then released.

The high-pressure solidified samples were coarse ground. We removed oil stains with ultrasonic cleaning, polished the surface of the samples with fine sandpaper and removed the residual polishing liquid on the surface with ultrasonic cleaning. The microstructures were observed using a Hitachi SU8010 scanning electron microscope (SEM) and Titan ETEM G2 transmission electron microscope (TEM). Energy dispersed X-ray spectroscopy (EDS) was used to analyze the distribution of elements by point and map scans. The phase composition was obtained using a Rigaku D/Max-RB X-ray diffractometer

(XRD) with a 20–90° diffraction angle range. JADE software was used to analyze the diffraction pattern. We used an Agilent G200 Nanoindenter with a Berkovich tip to load the sample. The indentation load and depth data were used in a constitutive equation to analyze the stress–strain relationship. We used a CHI660E series electrochemical workstation with a 3.5 % NaCl solution as the corrosion solution, a saturated mercuric chloride electrode as the reference electrode, and a platinum electrode as the counter electrode. We used a 1 mm thick sample embedded with copper wire as the working electrode. The test temperature was 26 °C, the scanning speed was 1 mV/s, and the scanning range was –1.5 to 1.5 V. After the open-circuit potential (OCP) was stable, we measured the Tafel curve and alternating current impedance spectrum (IMPS) of the CoCrFeNiAl_{0.2}Cu_{0.8} alloy. Corview and Zview software were used to analyze the Tafel curve and impedance spectrum, respectively.

3. Results and discussion

3.1. Microstructure and phase composition

Fig. 1 shows the microstructure morphology and phase composition of the CoCrFeNiAl_{0.2}Cu_{0.8} HEAs after solidification under three different pressures (ambient pressure, 4 GPa, and 7 GPa). Solidification at ambient pressure results in an HEA with gray and white columnar dendrites that have both primary branches and secondary dendrite arms (**Fig. 1a**). The matrix phase is shown in gray, while the intergranular phase is shown in white. When the HEAs are solidified under high pressure, the columnar dendrite features gradually disappear and the intergranular phase is intermittently broken up (**Fig. 1b** and **c**). The mass fraction of each HEA sample was measured using the Image-Pro Plus 6.0 image analysis system. Results indicate that the intergranular phase contents at ambient pressure, 4 GPa, and 7 GPa were 8.2 %, 5.7 %, and 5.4 %, respectively.

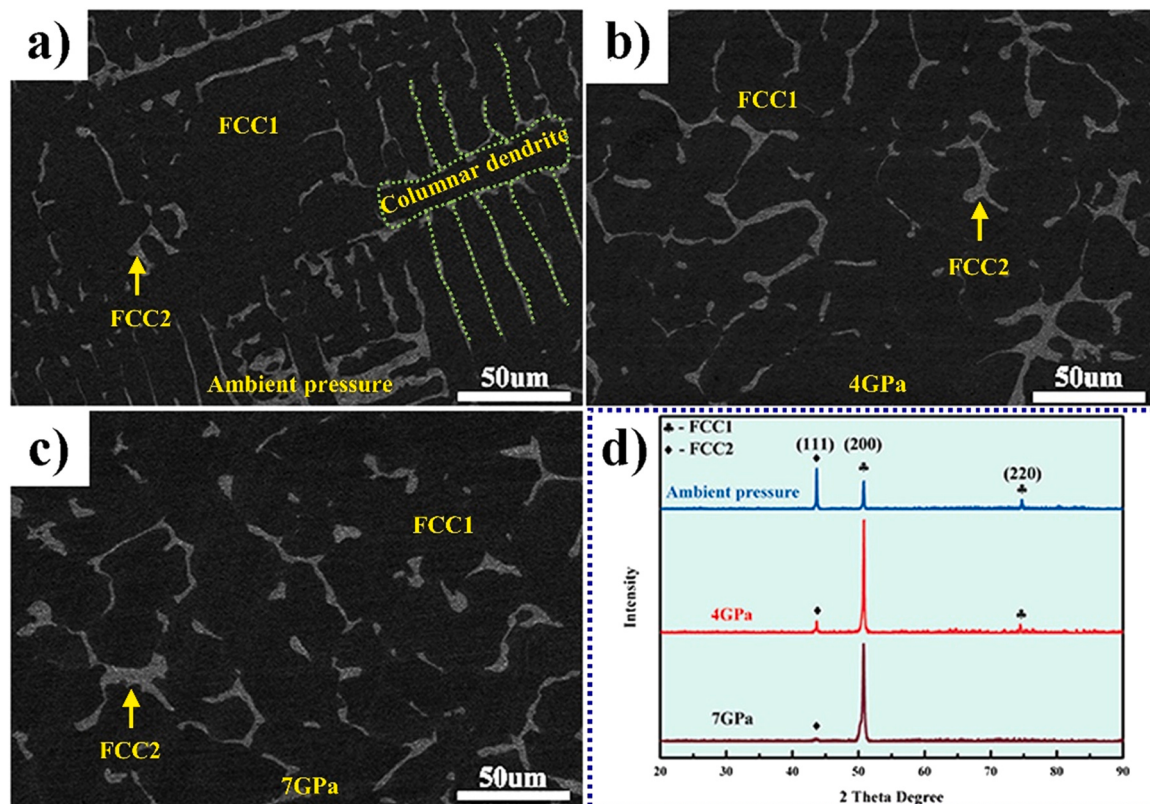


Fig. 1. Microstructure and phase composition of CoCrFeNiAl_{0.2}Cu_{0.8} HEA after solidification at various pressures (a) ambient pressure, (b) 4 GPa, (c) 7 GPa, (d) phase composition.

Table 1Corresponding parameters obtained by the calculation of Ω and the VEC criterion.

Alloy	Ω	Ω_p	δ	ΔH	ΔS	VEC
CoCrFeNiAl _{0.2} Cu _{0.8}	2.8	3.52	2.96 %	8.89	14.2	8.48

The X-ray diffraction patterns of the CoCrFeNiAl_{0.2}Cu_{0.8} HEAs indicate that the composition is a simple FCC solid solution phase and that no complex intermetallic compounds were precipitated (Fig. 1d). Table 1 shows the calculated values of the entropy-enthalpy quotient parameter (Ω), the valence electron concentration (VEC) criterion, and the mean square deviation of the atomic radius of elements (δ) of the CoCrFeNiAl_{0.2}Cu_{0.8} alloy. The results indicate that VEC = 8.48, Ω = 2.8, and δ = 2.96 %. These calculations confirm that the alloy was in the FCC phase. Note that there two forms of FCC structures are found in the CoCrFeNiAl_{0.2}Cu_{0.8} alloy, as shown in Fig. 1a-c.

Fig. 2 shows multiple high-resolution TEM (HRTEM) images of the CoCrFeNiAl_{0.2}Cu_{0.8} HEA solidified at ambient pressure. A section of the bright-field image of the matrix phase (Fig. 2a) was selected for HRTEM imaging (Fig. 2b). Fast Fourier transform (FFT) was performed on a portion of that image (Fig. 2c) and the corresponding inverse fast Fourier transform (IFFT) is shown in Fig. 2d. The FFT corresponds to the selected area electron diffraction (SAED) pattern along the [001] zone axis of the disordered FCC structure with an interplanar spacing of ~1.8 Å. Similarly, a portion of the bright-field image of the grain boundary (Fig. 2e) was chosen for HRTEM (Fig. 2f) and diffraction pattern (Fig. 2h) imaging. FFT was performed on a portion of the HRTEM image (Fig. 2g), while IFFT was performed on

the diffraction pattern (Fig. 2i). The FFT corresponds to the SAED pattern along the [001] zone axis of the ordered FCC structure with an interplanar spacing of ~3.65 Å. The elemental EDS maps (Fig. 2j-p) indicate that nanoparticles precipitated in the grain boundary and primarily comprised elemental Co, Cr, and Fe. Based on the XRD results, the intergranular and matrix phases correspond with the Cu-rich FCC2 and Fe-(Co, Cr)-rich FCC1 phases, respectively.

HRTEM images of the CoCrFeNiAl_{0.2}Cu_{0.8} HEA solidified at 7 GPa are shown in Fig. 3. The bright-field image of the grain boundary shows the detailed microstructure of the nano-precipitates (Fig. 3a). The HRTEM image of the nanoprecipitate phase is shown in Fig. 3b and FFT was performed on a section of that image (Fig. 3c). The corresponding IFFT is shown in Fig. 3d. The FFT corresponds to the SAED pattern along the [001] zone axis of the disordered FCC structure with an interplanar spacing of ~2.13 Å. The bright-field image of the matrix phase is shown in Fig. 3e and an HRTEM image was taken of a portion of that image (Fig. 3f). The corresponding FFT is shown in the inset (Fig. 3g). The FFT corresponds to the SAED pattern along the [001] zone axis of the disordered FCC structure with an interplanar spacing of ~1.8 Å. Results from the elemental mapping (Fig. 3j-p) indicate that the nanoparticles have precipitated in the Cu-rich FCC2 phase, and a bright-field image of the grain boundary (Fig. 3a) shows that the size of the nanoparticles ranges between 10 and 15 nm. As can be observed in Fig. 3d, the precipitates have a completely coherent relationship with the FCC2 phase, and they are too small to be observed clearly using map scanning.

When comparing the diffraction patterns of the three HEAs, there are diffraction peaks with the crystal plane indices of (111), (200), and (220) measured for the HEA solidified at ambient pressure.

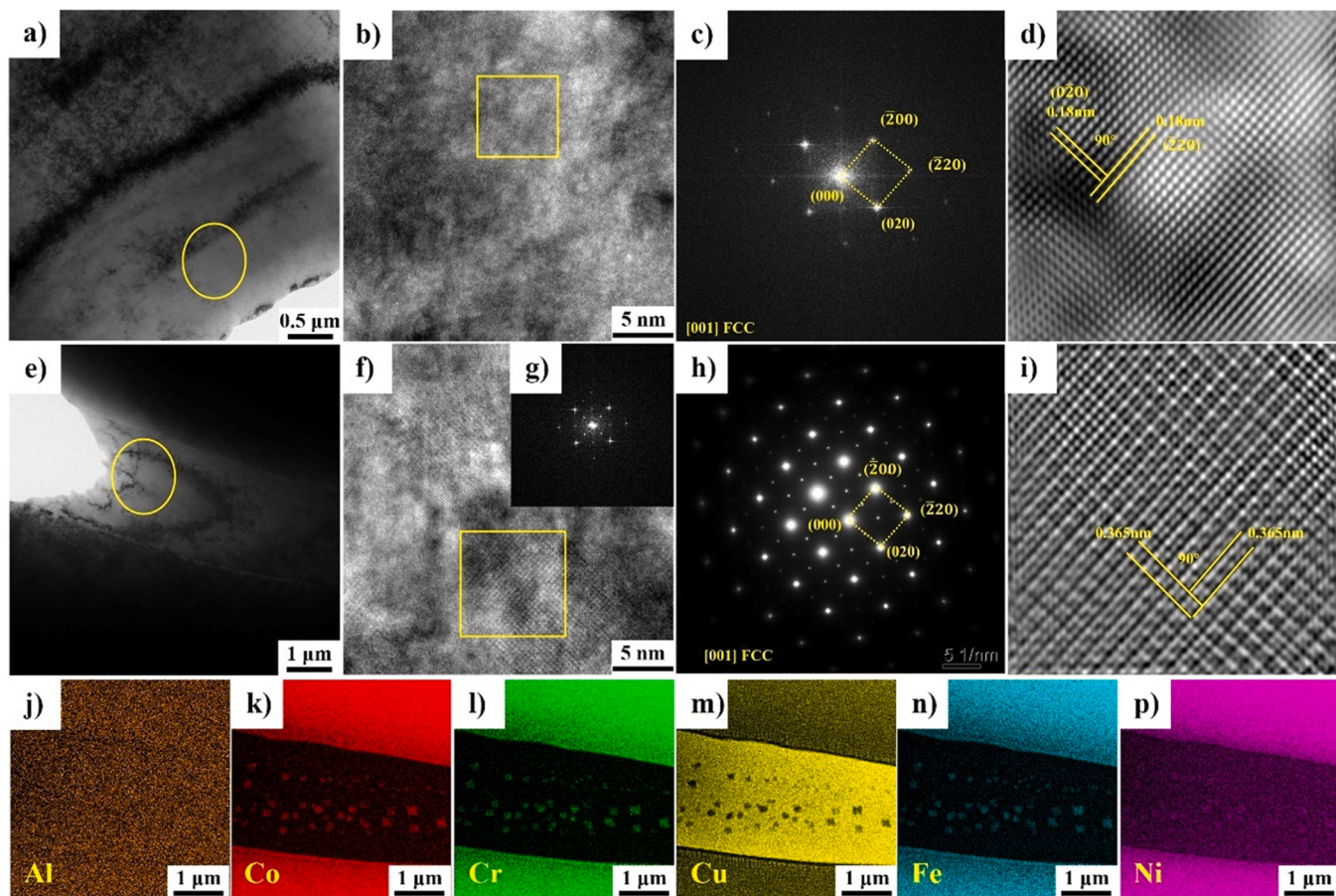


Fig. 2. HRTEM images of CoCrFeNiAl_{0.2}Cu_{0.8} HEA at ambient pressure (a) bright field image of the matrix phase; (b) HRTEM of the circled section in image (a); (c) FFT of the selected section in image (b); (d) IFFT of image (c); (e) bright field image of the GB; (f) HRTEM of the circled portion in image (e); (g) FFT of the selected section in image (f); (h) diffraction pattern of the circled portion in image (e); (i) IFFT of image (h); (j)–(p) elemental maps.

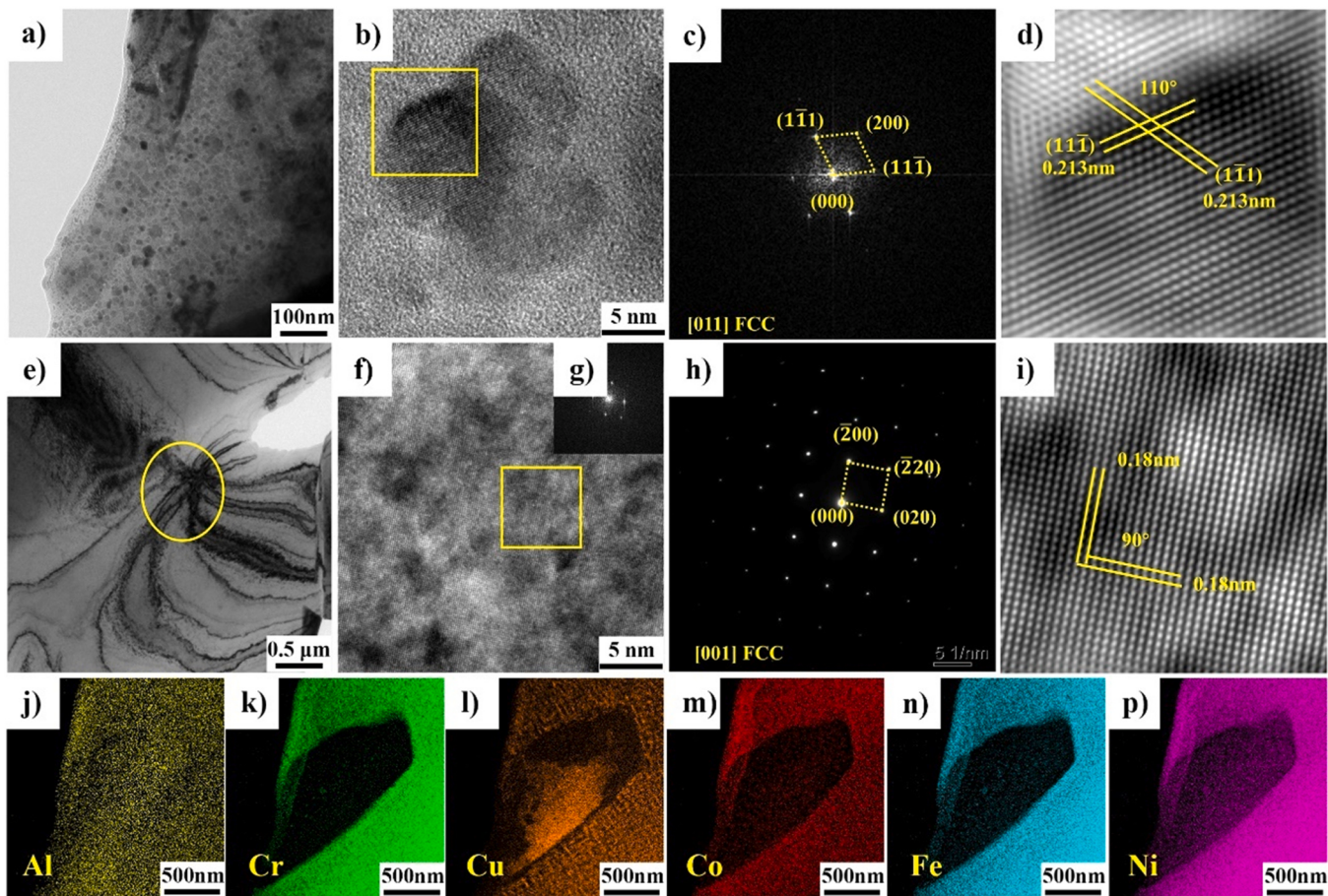


Fig. 3. HRTEM images of CoCrFeNiAl_{0.2}Cu_{0.8} HEA at 7 GPa (a) bright-field image of the GB; (b) HRTEM of the nano-precipitate phase; (c) FFT of the selected section in image (b); (d) IFFT of image (c); (e) bright-field image of the matrix, (f) HRTEM of the circled portion in image (e); (g) FFT of the selected section in image (f); (h) diffraction pattern of the circled portion in image (e); (i) IFFT of image (h); (j)–(p) elemental maps.

However, an increase in pressure causes a decrease in the diffraction peak intensity of the FCC2 phase. We used MDI's JADE software to perform quantitative analysis based on the reference intensity ratio (RIR) [33] reported on several PDF cards. Based on the XRD patterns and quantitative analysis, we can conclude that the content of the FCC2 phase decreases. However, the diffraction peak intensity of the FCC1 phase exhibited the opposite trend.

We further investigated the distribution of each element using elemental mapping and point scanning over the entire sample surface. Results are shown in Fig. 4 and Table 2. As shown in the elemental mapping images of the HEA prepared at ambient pressure, Cr, Co, and Fe are evenly distributed in the matrix phase (Fig. 4 b1, c1 and e1), while Al and Ni are evenly distributed throughout the entire interface (Fig. 4 a1 and f1). Conversely, Cu is segregated at the grain boundary (Fig. 4 d1). Results from the point scanning (Table 2) indicate that Cr, Co, Fe, and Ni exist in the FCC1 phase at similar atomic ratios, whereas the FCC2 phase is mostly composed of Cu and Ni. This is due to the weak affinity between Cu and the other five elements. The mixing enthalpies of Cu-Co, Cu-Cr, Cu-Fe, and Cu-Ni are 6, 12, 13, and 4 kJ/mol, respectively, making it thermodynamically challenging to mix Cu with other elements to form solid solutions. Therefore, Cu is pushed to the grain boundary when the alloy is solidified. The elemental mapping shows that the distribution of Al and Ni remained unchanged after high pressure solidification (Fig. 4 a2, a3, f2, and f3). However, it can be observed that the distribution of Cr, Co, and Fe in the FCC2 phase increased with increasing pressure (Fig. 4 b2, b3, c2, c3, e2, and e3). Although Cu was still enriched in the FCC2 phase, it had a lower degree of segregation (Fig. 4 d2 and

d3). The Cu content at the grain boundary gradually decreased with increasing pressure. As can be seen in Table 2, the composition of elements in the FCC1 and FCC2 phases remains nearly consistent across each pressure condition due to the influence of high pressure on the equilibrium distribution coefficient of the elements. Elements with equilibrium distribution coefficients less than 1 remain in the liquid phase during solidification, resulting in higher segregation. Conversely, elements with higher equilibrium partition coefficients are able to enter the solid phase during solidification, thus reducing the degree of segregation. Atomic diffusion is reduced in metals and alloys that are solidified under high pressure. This increases the solidification rate at the solid–liquid interface, which improves the equilibrium distribution coefficient and lowers the degree of element segregation.

3.2. Corrosion property characterization

Electrochemical impedance spectroscopy (EIS) was performed on the CoCrFeNiAl_{0.2}Cu_{0.8} HEAs after prepared under three different pressures (Fig. 5). The Nyquist plot, Bode plot, and equivalent circuit diagram are shown in Fig. 5a–c. The first circuit diagram (Fig. 5 c1) was used to fit the impedance spectrum of the HEA prepared at ambient pressure, while the second circuit diagram (Fig. 5 c2) was used for the HEAs prepared at high pressures. Results of the fitted impedance data are shown in Fig. 5d. The Nyquist curve fitted by the equivalent circuit diagram indicates that the established charge transfer process model can predict the corrosion behavior of CoCrFeNiAl_{0.2}Cu_{0.8} HEAs under various pressures, confirming the

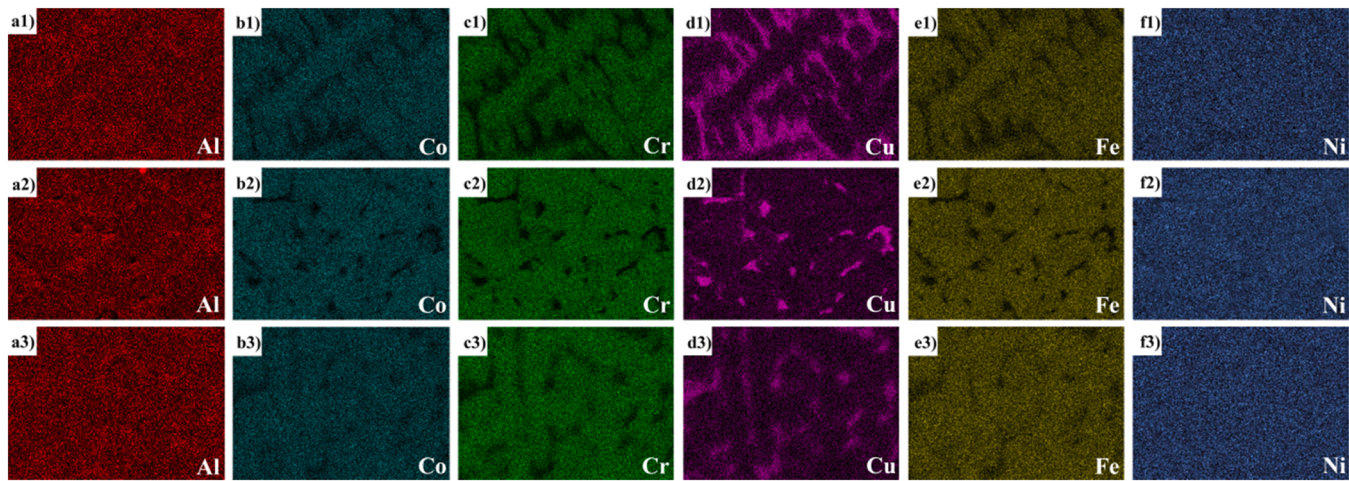


Fig. 4. Elemental mapping images of CoCrFeNiAl_{0.2}Cu_{0.8} HEAs prepared at three different pressures (a1)–(f1) ambient pressure, (a2)–(f2) 4 GPa, and (a3)–(f3) 7 GPa.

Table 2
Point-scanning results of CoCrFeNiAl_{0.2}Cu_{0.8} HEAs at various pressures.

Pressure	Phase	Co/at%	Cr/at%	Fe/at%	Cu/at%	Ni/at%	Al/at%
Ambient pressure	FCC1	22.7	20.78	22.46	10.36	19.28	4.42
	FCC2	5.64	9.27	3.00	58.88	15.63	7.57
4 GPa	FCC1	22.45	20.7	21.38	11.43	20.31	3.74
	FCC2	9.9	6.95	10.21	48.88	17.83	6.46
7 GPa	FCC1	21.84	20.44	20.65	11.64	22.45	2.95
	FCC2	14.55	12.93	13.39	39.75	18.39	1.00

proposed experimental results. The fitting parameters of the CoCrFeNiAl_{0.2}Cu_{0.8} HEAs under two different pressures are listed in **Table 3**. We observed a single capacitive impedance loop. Note that the size of the CoCrFeNiAl_{0.2}Cu_{0.8} HEA capacitor curves increases with increasing solidification pressure, which suggests that there is higher corrosion resistance at high solidification pressure. The Bode plot shows phase angles of approximately 70° for the HEAs prepared at both ambient pressure and 4 GPa over a wide frequency range, whereas the phase angle for the HEA prepared at 7 GPa is

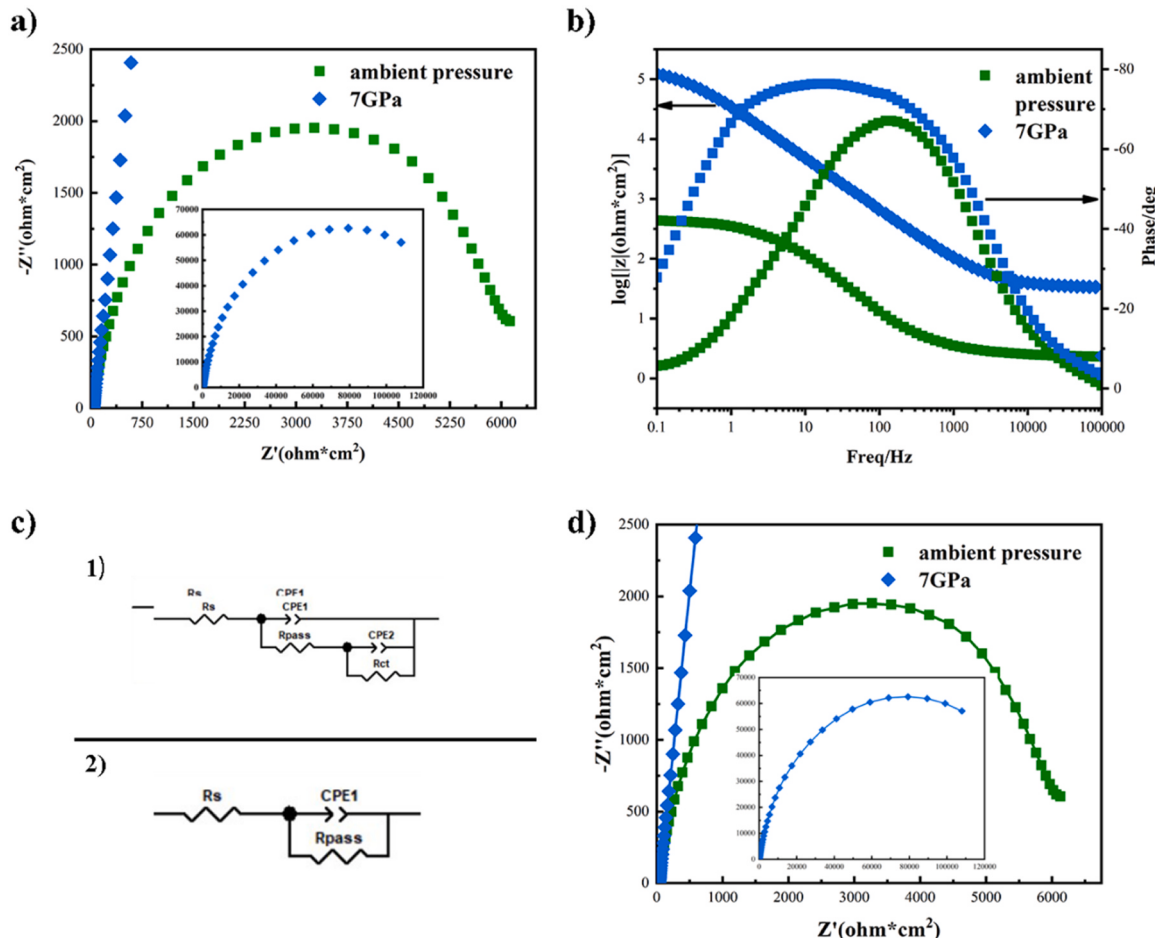


Fig. 5. EIS of CoCrFeNiAl_{0.2}Cu_{0.8} HEAs solidified at various pressures (a) Nyquist plots, (b) Bode plots, (c) the EIS spectrum equivalent circuit, and (d) fitting results.

Table 3

Fitting values of the equivalent circuits of the CoCrFeNiAl_{0.2}Cu_{0.8} HEAs solidified at various pressures.

	R _S Ω cm ²	CPE1-T μF cm ⁻²	CPE1-P	R _{pass} Ω cm ²	CPE2-T μF cm ⁻²	CPE2-P	R _{ct} Ω·cm ²
Ambient pressure	33.11	8.91E-06	0.85	2058	7.31E-05	0.75	4134
7 GPa	34.24	5.75E-06	0.86	149,500	–	–	–

approximately 80°. This result indicates that the 7 GPa HEA has a high resistance value and forms a passive film. **Table 3** also shows that the passive resistance (R_{pass}) of the ambient pressure HEA is lower than the charge-transfer resistance (R_{ct}) due to the oxide in the corrosion pit reaching a thickness where it has adequate protection; however, if the passive film is rich in Cu, that protective effect decreases. R_S and R_{pass} for the 7 GPa are greater than the values of ambient pressure. For example, the R_{pass} for the 7 GPa HEA is 71.64 times that of the ambient pressure HEA, indicating that the ionization process of the HEA in the electrochemical experiment is inhibited with an increase in solidification pressure. A higher R_{ct} value means that the alloy is more resistant to corrosion reactions, and therefore, has a lower corrosion rate and higher corrosion resistance.

The potentiodynamic polarization curve and corrosion morphology of the CoCrFeNiAl_{0.2}Cu_{0.8} HEAs solidified at various pressures are shown in **Fig. 6**. The Tafel method was used to derive the key electrochemical parameters shown in **Table 4**, such as the corrosion current density (I_{corr}) and corrosion potential (E_{corr}). The CoCrFeNiAl_{0.2}Cu_{0.8} HEA solidified at 7 GPa has an I_{corr} value that is approximately 85.4 % lower than that of CoCrFeNiAl_{0.2}Cu_{0.8} HEA solidified at ambient pressure, which can be considered a significant improvement [34]. Additionally, the anode area (β_a) increases with increasing solidification pressure, which further confirms better corrosion resistance at high pressure. The E_{corr} value is used to determine the corrosion tendency of alloys. According to thermodynamic principles, lower E_{corr} values have greater corrosion tendencies. The E_{corr} of the 7 GPa HEA is -0.76, which is approximately 9.8 % greater than that of the ambient pressure HEA, confirming that the corrosion tendency of the 7 GPa HEA is lower than that of the ambient pressure HEA. An increase in solidification pressure resulted in alloy microstructure refinement, increased specific surface area of the alloy, and increased corrosion contact

area of the corresponding unit. We also observed a decreased E_{corr} value and higher corrosion tendency with higher solidification pressure. Grain refinement causes an increase in the number of grain boundaries and initial passive film nucleation positions. Grain boundaries and dislocations can also act as a driving force for the growth of passive films. An increase in defect density can promote the formation of a denser passive film on the surface of the material, thereby reducing its corrosion rate and increasing its corrosion resistance. **Fig. 6** shows an obvious passivation platform observed on the high pressure HEA. The corrosion resistance is directly related to the corrosion rate, which can be calculated using the following equation:

$$CR = \frac{I_{corr} * K * EW}{d * A} \quad (1)$$

where I_{corr} is the corrosion current density (A/cm²), K is the corrosion rate constant (3.27 * 10³ mm/y), EW is the equivalent weight (g), d is the density of the metal (g/cm³), and A is the surface area (cm²). Based on the calculated results (**Table 4**), the corrosion rates of the ambient pressure and 7 GPa HEAs are 2.5 × 10⁻³ and 3.6 × 10⁻⁴ mA/a, respectively. The corrosion rate of the 7 GPa HEA is approximately 85.6 % lower than that of the ambient pressure HEA, further proving that high pressure solidification can improve the corrosion resistance of the alloy. According to Fan et al. [35], the corrosion resistance of CoCrFeNiAlCu solidified under high pressure was significantly improved and achieved the best corrosion resistance compared to other alloys with the same elements.

After the potentiodynamic polarization test, the corrosion surface morphology was observed using SEM (**Fig. 6b** and **c**). As shown in **Fig. 6a**, there is obvious surface corrosion over the entire surface of the ambient pressure HEA with a high degree of grain boundary corrosion, particularly at the Cu segregation grain boundary.

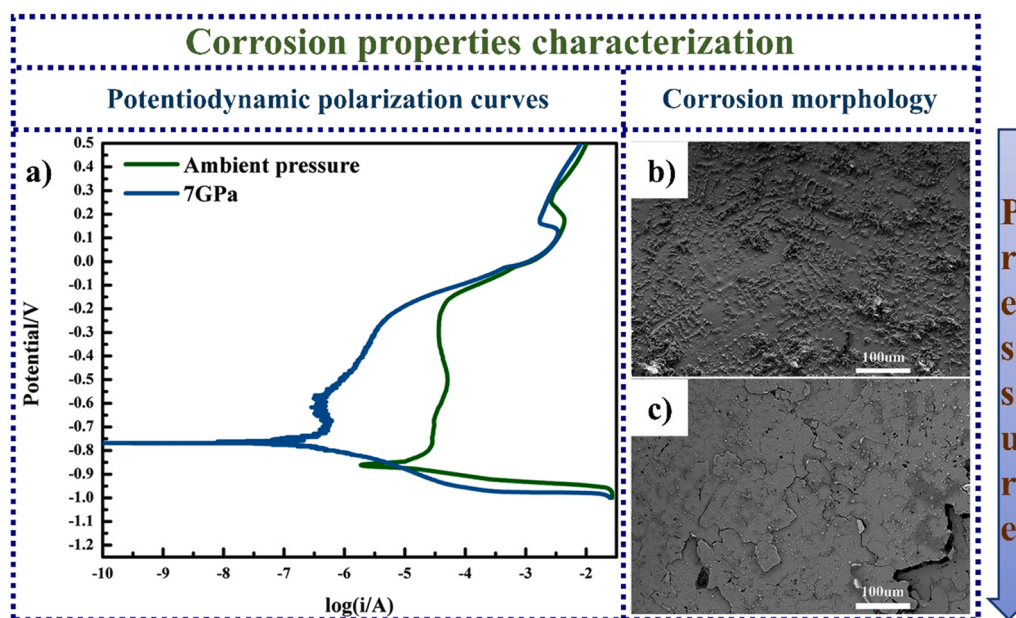


Fig. 6. Corrosion property characterization for CoCrFeNiAl_{0.2}Cu_{0.8} HEAs at various pressures (a) potentiodynamic polarization curves, (b) corrosion morphology at ambient pressure, and (c) corrosion morphology at 7 GPa.

Table 4

Key electrochemical parameters of CoCrFeNiAl_{0.2}Cu_{0.8} HEAs at various pressures.

Pressure	I_{corr} (A/cm ²)	E_{corr} (V)	β_a	β_c	Corrosion rate (mA/y)
Ambient pressure	7.6421×10^{-7}	-0.8455	0.20052	-0.03627	2.5×10^{-3}
7 GPa	1.1095×10^{-7}	-0.7624	0.35074	-0.08692	3.6×10^{-4}

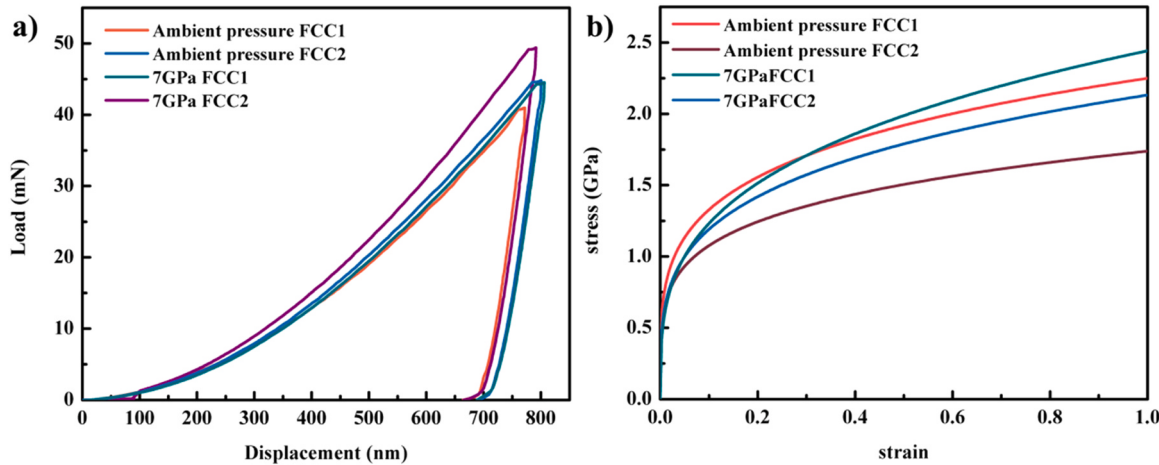


Fig. 7. Nanoindentation of CoCrFeNiAl_{0.2}Cu_{0.8} HEA after solidified at various pressures (a) load-displacement (p-h) curves and b) stress–strain curves.

However, the surface of the CoCrFeNiAl_{0.2}Cu_{0.8} HEA solidified at 7 GPa remains smooth, with only a small amount of pitting and grain boundary corrosion. These observations indicate that the corrosion resistance of the alloy is improved by controlling the Cu segregation using high pressure.

3.3. Characterization of mechanical properties and the constitutive relationship between stress and strain

The nanoindentation load–displacement (P-h) curves of the FCC1 and FCC2 phases of the CoCrFeNiAl_{0.2}Cu_{0.8} HEA solidified at various pressures are shown in Fig. 7a. The P-h curves of each micro-region have similar loading, maintenance, and unloading trends. In the initial stage of loading, the indentation depth increased rapidly with increasing load, and as loading progressed, the increase up to the maximum load became more gradual. The FCC2 phase of the 7 GPa HEA had the largest load and was quite different from the FCC1 phase. According to the method proposed by G. Cheng et al. [36], the curvature (C) of the loading stage is calculated as follows:

$$C = \frac{p}{h^2} \quad (2)$$

where p and h are the indentation load and depth, respectively. The representative stress ($\sigma_{0.033}$) is expressed using the following equation:

$$\frac{C}{\sigma_{0.033}} = -1.131 \times \left[\ln \left(\frac{E_r}{\sigma_{0.033}} \right) \right]^3 + 13.635 \times \left[\ln \left(\frac{E_r}{\sigma_{0.033}} \right) \right]^2 - 30.594 \times \left[\ln \left(\frac{E_r}{\sigma_{0.033}} \right) \right] + 29.467 \quad (3)$$

where E_r is the reduced modulus and σ_y is the yield strength.

After parameters E , σ_y , and $\sigma_{0.033}$ are determined, the hardening exponent (n) can be calculated as follows:

$$\sigma_{0.033} = \sigma_y \left(1 + 0.033 \times \frac{E}{\sigma_y} \right)^n \quad (4)$$

Table 5
Reverse calculation results.

Phase	Hardness (GPa)	E (GPa)	σ_y (MPa)
Ambient pressure FCC1	3.42	189.3	470.8
Ambient pressure FCC2	3.97	158.2	513.5
7 GPa FCC1	3.79	179.1	482.7
7 GPa FCC2	4.36	150.1	623.1

The stress–strain constitutive relationship of each phase was calculated using Eqs. (2)–(4) and the load–displacement curve (Fig. 7b). The corresponding calculated parameters are listed in Table 5, and indicate that the hardness of the ambient pressure HEA's FCC1 and FCC2 phases are 3.42 GPa and 3.97 GPa, respectively. In comparison, the hardness of the 7 GPa HEA's FCC1 and FCC2 phases are 3.79 GPa and 4.36 GPa, respectively. The hardness values of the FCC1 phase thus increased by 10.8 % with an increase in solidification pressure, while the FCC2 phase hardness increased by 9.8 %. The elastic modulus of the 7 GPa HEA's FCC1 and FCC2 phases are 179.1 GPa and 150.1 GPa, respectively. As can be seen, the elastic modulus of the FCC1 and FCC2 phases decreased by 5.4 % and 5.1 %, respectively, with an increase in pressure. The yield strengths of the ambient pressure HEA's FCC1 and FCC2 phases are 470.8 MPa and 513.5 MPa, respectively, while the yield strengths of the 7 GPa HEA's FCC1 phase and FCC2 phases are 482.7 MPa and 623.1 MPa, respectively. The yield strengths of the FCC1 and FCC2 phases thus increased by 2.5 % and 21.3 %, respectively, with an increase in solidification pressure. The increase in FCC1 phase strength is caused by high pressure altering the atom spacing [37], which can cause significant lattice deformation, lead to dislocation reproduction, and hinder dislocations slippage. The FCC2 phase is thus stronger than the FCC1 phase, and also more affected by an increase in solidification pressure. This strengthening is attributed to nano-precipitation and dispersive strengthening observed via TEM analysis.

During solidification under ambient pressure, the solid solubility of Co, Cr, and Fe in the Cu-rich FCC2 phase gradually decreases with decreasing temperature. The binary equilibrium phase diagrams of Cu-Co, Cu-Cr, and Cu-Fe indicate that their solid solubility with Cu is close to 0 at 25 °C. As solidification proceeds, the excess Co, Cr, and Fe elements in

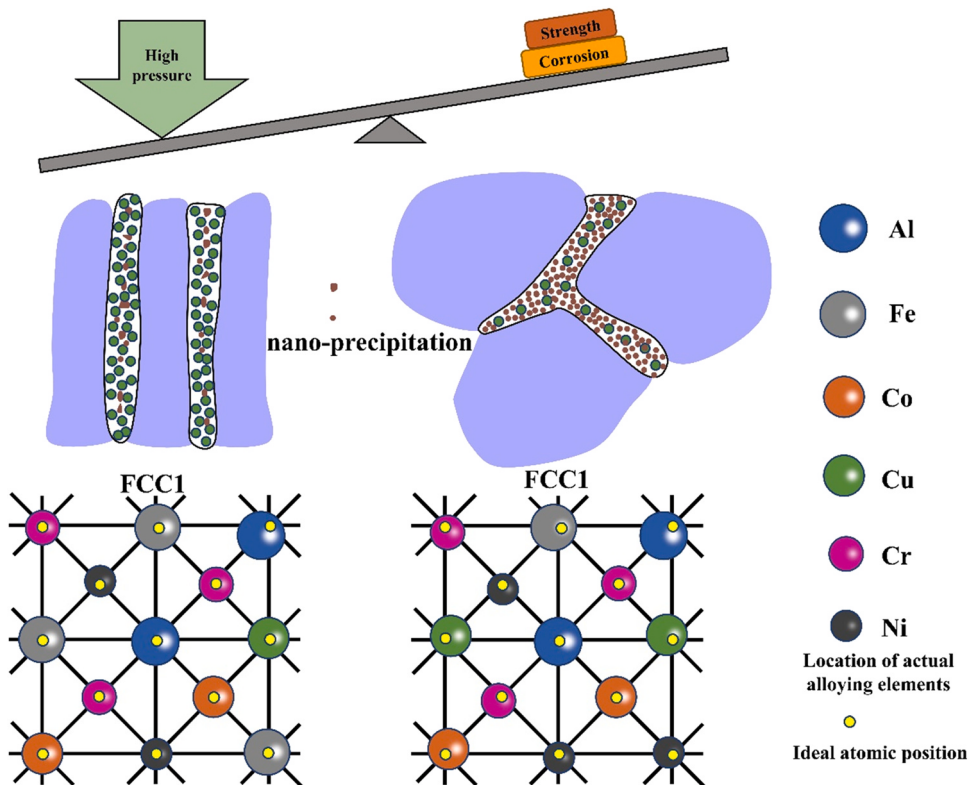


Fig. 8. Mechanistic diagram of the correlation between the microstructure and properties at high and low pressures.

the FCC2 phase precipitate and the elements at the interface will directly diffuse into the FCC1 phase. Eventually, the elements diffuse to the middle region of the FCC2 phase and will form nano-precipitates, which play the role of nano-enhancement. In comparison, during the initial stage of high-pressure solidification, more Co, Cr, and Fe are dissolved into the FCC2 phase and precipitate in the continuous solidification process. Elemental diffusion is significantly inhibited under high pressure, and therefore, a smaller and higher dispersed nano-precipitated phase forms. During this process, both nano-precipitation and dispersive strengthening occur, and the strength of the FCC2 phase improves significantly. The improved corrosion resistance, strength, and hardness of the high-pressure CoCrFeNiAl_{0.2}Cu_{0.8} HEA can be attributed to the weakening of the Cu-enriched FCC2 phase at the grain boundary and the increase in lattice distortion in the solid solution. The corresponding mechanism is shown in Fig. 8.

4. Conclusions

In this study, we investigated the microstructure evolution, element distribution, corrosion properties, and mechanical properties of CoCrFeNiAl_{0.2}Cu_{0.8} HEAs prepared at various pressures. Based on the results of this study, we proposed a mechanism to improve the properties of this high-pressure alloy. The main conclusions are summarized as follows.

- 1) The CoCrFeNiAl_{0.2}Cu_{0.8} HEA solidified at ambient pressure exhibited a columnar dendrite structure with the Cu-rich FCC2 phase segregated between dendrites. After high-pressure solidification (4 and 7 GPa), the microstructure gradually changed to be an equiaxed crystal. The increase in solidification pressure resulted in an increase in the volume fraction of the FCC1 phase and refinement of the grains. There was also a decrease in the Cu-rich FCC2 phase as well as Cu segregation.
- 2) Nano-precipitation occurred in the FCC2 phase at ambient pressure solidification, which played a role in nano-enhancement.

High-pressure solidification resulted in finer and more dispersed nano-precipitation, which caused simultaneous nano-enhancement and dispersion strengthening.

- 3) The potentiodynamic polarization curves indicated that the corrosion rate of the HEA prepared using high solidification pressure was reduced by 85.6 % compared to the HEA prepared with ambient pressure solidification. IMP showed that the high-pressure CoCrFeNiAl_{0.2}Cu_{0.8} HEA had a lower corrosion rate and greater resistance than the HEA prepared using ambient pressure solidification.
- 4) The hardness values of the FCC1 and FCC2 phases increased by 10.8 % and 9.8 %, respectively, with an increase in solidification pressure. The yield strength of each phase also increased with an increase in solidification pressure.

CRedit authorship contribution statement

Xiaohong Wang: Conceptualization, Methodology, Software, Writing – original draft. **Huiqing Xie:** Data curation, Writing – original draft. **Yulei Deng:** Visualization, Investigation. **Dongdong Zhu:** Supervision, Funding acquisition, Writing – review & editing. **Xing Yang:** Software, Validation. **Duo Dong:** Methodology, Software. **Tengfei Ma:** Project administration, Writing – review & editing.

Data Availability

No data was used for the research described in the article.

Declaration of Competing Interest

The authors declare that they have no known competing financial interests or personal relationships that could have appeared to influence the work reported in this paper.

Acknowledgments

This work was supported by the Zhejiang Province Natural Science Foundation of China [No. LQ20E010003], the National Natural Science Foundation of China [Nos. 52271106, 52071188, 52171120, 52001262] and Research Funding Project of Education Department of Zhejiang Province (No. Y202045618).

References

- [1] L. Chen, A. Jarlöv, H.L. Seet, M.L.S. Nai, Y. Li, K. Zhou, Exploration of V-Cr-Fe-Co-Ni high-entropy alloys with high yield strength: a combination of machine learning and molecular dynamics simulation, *Comp. Mater. Sci.* 217 (2023) 111888, <https://doi.org/10.1016/j.commatsci.2022.111888>
- [2] F. Maresca, W.A. Curtin, Mechanistic origin of high strength in refractory BCC high entropy alloys up to 1900K, *Acta Mater.* 182 (2020) 235–249, <https://doi.org/10.1016/j.actamat.2019.10.015>
- [3] M. He, H. Kang, S. Lin, Y. Liu, P. Zhang, W. Qin, X. Wu, Impressive high-temperature oxidation resistance of FeCrNiMnAl high entropy alloy coating on the ferritic/martensitic steel with primordial Al_2O_3 and Mn_2O_4 gradient films, *J. Alloy Compd.* 928 (2022) 167109, <https://doi.org/10.1016/j.jallcom.2022.167109>
- [4] A.O. Moghaddam, M. Sudarikov, N. Shaburova, D. Zherebtsov, V. Zhivulin, I.A. Solizoda, A. Starikov, S. Veselkov, O. Samoilova, E. Trofimov, High temperature oxidation resistance of W-containing high entropy alloys, *J. Alloy Compd.* 897 (2022) 162733, <https://doi.org/10.1016/j.jallcom.2021.162733>
- [5] A.O. Moghaddam, N.A. Shaburova, M.V. Sudarikov, S.N. Veselkov, O.V. Samoilova, E.A. Trofimov, High temperature oxidation resistance of $\text{Al}_{0.25}\text{CoCrFeNiMn}$ and $\text{Al}_{0.45}\text{CoCrFeNiSi}_{0.45}$ high entropy alloys, *Vacuum* 192 (2021) 110412, <https://doi.org/10.1016/j.vacuum.2021.110412>
- [6] J. Wang, Z. Zhang, H. Dai, H. Fujiwara, X. Chen, K. Ameyama, Enhanced corrosion resistance of CoCrFeMnNi high entropy alloy using heterogeneous structure design, *Corros. Sci.* 209 (2022) 110761, <https://doi.org/10.1016/j.corsci.2022.110761>
- [7] Z.C. Zhang, A.D. Lan, M. Zhang, J.W. Qiao, Effect of Ce on the pitting corrosion resistance of non-equiautomic high-entropy alloy $\text{Fe}_{40}\text{Mn}_{20}\text{Cr}_{20}\text{Ni}_{20}$ in 3.5wt% NaCl solution, *J. Alloy Compd.* 909 (2022) 164641, <https://doi.org/10.1016/j.jallcom.2022.164641>
- [8] J. Xu, S. Peng, Z. Li, S. Jiang, Z.H. Xie, P. Munroe, H. Lu, Remarkable cavitation erosion-corrosion resistance of CoCrFeNiTiMo high-entropy alloy coatings, *Corros. Sci.* 190 (2021) 109663, <https://doi.org/10.1016/j.corsci.2021.109663>
- [9] Y. Huang, Y. Hu, M. Zhang, C. Mao, Y. Tong, J. Zhang, K. Li, K. Wang, On the enhanced wear resistance of laser-clad CoCrCuFeNiTi_x high-entropy alloy coatings at elevated temperature, *Tribol. Int.* 174 (2022) 107767, <https://doi.org/10.1016/j.triboint.2022.107767>
- [10] P. Moazzeni, M.R. Toroghinejad, P. Cavaliere, Effect of Iron content on the microstructure evolution, mechanical properties and wear resistance of Fe_xCoCrNi high-entropy alloy system produced via MA-SPS, *J. Alloy Compd.* 870 (2021) 159410, <https://doi.org/10.1016/j.jallcom.2021.159410>
- [11] Q. Xing, A.C. Feltrin, F. Akhtar, Processing, microstructure and high temperature dry sliding wear of a Cr-Fe-Hf-Mn-Ti-Ta-V high-entropy alloy based composite, *Mater. Today Commun.* 28 (2021) 102657, <https://doi.org/10.1016/j.mtcomm.2021.102657>
- [12] A.C. Martin, J.P. Oliveira, C. Fink, Elemental effects on weld cracking susceptibility in $\text{Al}_{x}\text{CoCrCuYFeNi}$ high-entropy alloy, *Met. Mater. Trans. S* 51 (2020) 778–787, <https://doi.org/10.1007/s11661-019-05564-8>
- [13] C. Meng, Z. Song, X. Qiu, G. Wang, C. Wu, X. Ren, W. Zhuang, X. Wang, Effect of Cu content on microstructure and properties of CoCrFeNiCu_x high-entropy alloy coatings prepared by induction cladding, *J. Alloy Compd.* 934 (2023) 167896, <https://doi.org/10.1016/j.jallcom.2022.167896>
- [14] L. Huang, X. Wang, B. Huang, X. Zhao, H. Chen, C. Wang, Effect of Cu segregation on the phase transformation and properties of AlCrFeNiTiCu_x high-entropy alloys, *Intermetallics* 140 (2022) 107397, <https://doi.org/10.1016/j.intermet.2021.107397>
- [15] X. Hao, H. Dong, Y. Xia, P. Li, Microstructure and mechanical properties of laser welded TC4 titanium alloy/304 stainless steel joint with $(\text{CoCrFeNi})_{100-x}\text{Cu}_x$ high entropy alloy interlayer, *J. Alloy Compd.* 803 (2019) 649–657, <https://doi.org/10.1016/j.jallcom.2019.06.225>
- [16] J. Wang, Y. Chen, Y. Zhang, W. Dai, Q. Xu, W. Li, Y. Liu, Corrosion and slurry erosion wear performances of coaxial direct laser deposited CoCrFeNiCu_{1-x}Mo_x high-entropy coatings by modulating the second-phase precipitation, *Mater. Des.* 212 (2021) 110277, <https://doi.org/10.1016/j.matdes.2021.110277>
- [17] H. Zheng, R. Chen, G. Qin, X. Li, Y. Su, H. Ding, J. Guo, H. Fu, Microstructure evolution, Cu segregation and tensile properties of CoCrFeNiCu high entropy alloy during directional solidification, *J. Mater. Sci. Technol.* 38 (2020) 19–27, <https://doi.org/10.1016/j.jmst.2019.08.019>
- [18] M. Vaidya, K.G. Pradeep, B.S. Murty, G. Wilde, S.V. Divinski, Bulk tracer diffusion in CoCrFeNi and CoCrFeMnNi high entropy alloys, *Acta Mater.* 146 (2018) 211–224, <https://doi.org/10.1016/j.actamat.2017.12.052>
- [19] X. Chen, H. Qian, Y. Lou, B. Yang, T. Cui, D. Zhang, Effects of Cu-content and passivation treatment on the corrosion resistance of $\text{Al}_{0.3}\text{Cu}_x\text{CoCrFeNi}$ high-entropy alloys, *J. Alloy Compd.* 920 (2022) 165956, <https://doi.org/10.1016/j.jallcom.2022.165956>
- [20] E.H. Bartawi, O.V. Mishin, G. Shaban, J.H. Nordlien, R. Ambat, Electron microscopy analysis of grain boundaries and intergranular corrosion in aged Al-Mg-Si alloy doped with 0.05 wt% Cu, *Corros. Sci.* 209 (2022) 110758, <https://doi.org/10.1016/j.corsci.2022.110758>
- [21] Y. Zou, Q. Liu, Z. Jia, Y. Xing, L. Ding, X. Wang, The intergranular corrosion behavior of 6000-series alloys with different Mg/Si and Cu content, *Appl. Surf. Sci.* 405 (2017) 489–496, <https://doi.org/10.1016/j.apsusc.2017.02.045>
- [22] K. Shimizu, K. Nisanicoglou, High resolution SEM investigation of intercrystalline corrosion on 6000-series aluminum alloy with low copper content, *ECS Electrochem. Lett.* 3 (2014) C29–C31, <https://doi.org/10.1149/2.0041409eel>
- [23] C. Ji, A. Ma, J. Jiang, Mechanical properties and corrosion behavior of novel Al-Mg-Zn-Cu-Si lightweight high entropy alloys, *J. Alloy Compd.* 900 (2022) 163508, <https://doi.org/10.1016/j.jallcom.2021.163508>
- [24] X. Zhang, Y. Lv, T. Hashimoto, J.O. Nilsson, X. Zhou, Intergranular corrosion of AA6082 Al-Mg-Si alloy extrusion: the influence of trace Cu and grain boundary misorientation, *J. Alloy Compd.* 853 (2021) 157228, <https://doi.org/10.1016/j.jallcom.2020.157228>
- [25] Z.S. Nong, H.Y. Wang, J.C. Zhu, First-principles calculations of structural, elastic and electronic properties of $(\text{TaNb})_{0.67}(\text{HfZrTi})_{0.33}$ high-entropy alloy under high pressure, *Int. J. Min. Mater.* 27 (2020) 1405–1414, <https://doi.org/10.1007/s12613-020-2095-z>
- [26] X. Lin, P. Dai, C. Xu, D. Fang, K. Guo, Z. Ren, Solute redistribution and mechanism of structure refinement of Mg-Al alloy during solidification under high pressure, *J. Alloy Compd.* 910 (2022) 164777, <https://doi.org/10.1016/j.jallcom.2022.164777>
- [27] M. Li, X. Zhao, G. Shao, H. Wang, J. Zhu, W. Liu, B. Fan, H. Xu, H. Lu, Y. Zhou, R. Zhang, Oscillatory pressure sintering of high entropy $(\text{Zr}_{0.2}\text{Ta}_{0.2}\text{Nb}_{0.2}\text{Hf}_{0.2}\text{Mo}_{0.2})\text{B}_2$ ceramic, *Ceram. Int.* 47 (2021) 8707–8710, <https://doi.org/10.1016/j.ceramint.2020.11.108>
- [28] Q.L. Cao, P.P. Wang, J.X. Shao, F.H. Wang, Transport properties and entropy-scaling laws for diffusion coefficients in liquid $\text{Fe}_{0.9}\text{Ni}_{0.1}$ up to 350 GPa, *RSC Adv.* 6 (2016) 84420–84425, <https://doi.org/10.1039/C6RA15211B>
- [29] R. Zhang, C. Zou, Z. Wei, H. Wang, In situ formation of SiC in Al–40Si alloy during high-pressure solidification, *Ceram. Int.* 47 (2021) 24485–24493, <https://doi.org/10.1016/j.ceramint.2021.05.164>
- [30] K. Guo, C. Xu, X. Lin, J. Ye, C. Zhang, D. Huang, Microstructure and strengthening mechanism of Mg-5.88Zn-0.53Cu-0.16Zr alloy solidified under high pressure, *Trans. Nonferrous Met. Soc.* 30 (2020) 99–109, [https://doi.org/10.1016/S1003-6326\(19\)65183-6](https://doi.org/10.1016/S1003-6326(19)65183-6)
- [31] T. Chang, C.M. Zou, D.D. Zhu, X.H. Wang, Z.J. Wei, H.W. Wang, N. Fang, J.H. Chen, The evolution of microstructure, micromechanical and magnetic properties of FeCoNiAlSi alloys with peritectic structure processed by high-pressure solidification, *J. Alloy Compd.* 920 (2022) 165958, <https://doi.org/10.1016/j.jallcom.2022.165958>
- [32] T. Chang, C.M. Zou, D.D. Zhu, X.H. Wang, Z.J. Wei, H.W. Wang, N. Fang, J.H. Chen, The evolution of microstructure, micromechanical and magnetic properties of FeCoNiSi alloys solidified under high pressure, *Mater. Charact.* 189 (2022) 112009, <https://doi.org/10.1016/j.matchar.2022.112009>
- [33] S.Y. Liao, R. Yao, X.Y. Chen, G.R. Wang, F. Zheng, Structure refinement and up-conversion of $\text{Ho}^{3+}/\text{Er}^{3+}$ Co-doped $12\text{CaO}\cdot7\text{Al}_2\text{O}_3$, *Mater. Des.* 108 (2016) 93–105, <https://doi.org/10.1016/j.matdes.2016.06.079>
- [34] Q.L. Cao, P.P. Wang, D.H. Huang, J.S. Yang, M.J. Wan, F.H. Wang, Properties of liquid nickel along melting lines under high pressure, *Chin. Phys. Lett.* 32 (2015) 086201, <https://doi.org/10.1088/0256-307X/32/8/086201>
- [35] Q. Fan, C. Chen, C. Fan, Z. Liu, X. Cai, S. Lin, C. Yang, Ultrasonic suppression of element segregation in gas tungsten arc cladding AlCoCuFeNi high-entropy alloy coatings, *Surf. Coat. Technol.* 420 (2021) 127364, <https://doi.org/10.1016/j.surfcoat.2021.127364>
- [36] G. Cheng, K.S. Choi, X. Hu, X. Sun, Determining individual phase properties in a multi-phase Q&P steel using multi-scale indentation tests, *Mater. Sci. Eng.* 652 (2016) 384–395, <https://doi.org/10.1016/j.msea.2015.11.072>
- [37] B. Cheng, H. Lou, A. Sarkar, Z. Zeng, F. Zhang, X. Chen, L. Tan, K. Glazyrin, H.P. Hiermann, J. Yan, L. Wang, R. Djedanovic, H. Hahn, Q. Zeng, Lattice distortion and stability of $(\text{Co}_{0.2}\text{Cu}_{0.2}\text{Mg}_{0.2}\text{Ni}_{0.2}\text{Zn}_{0.2})\text{O}$ high-entropy oxide under high pressure, *Mater. Today Adv.* 8 (2020) 100102, <https://doi.org/10.1016/j.mtadv.2020.100102>